

The Nature of the Halo Population of NGC 5128 Resolved with NICMOS on the *Hubble Space Telescope*

Francine R. Marleau

*Institute of Astronomy, University of Cambridge, Madingley Road,
Cambridge CB3 0HA, England, U.K.*

James R. Graham

*Department of Astronomy, University of California, Berkeley,
Campbell Hall, Berkeley, CA 94720, USA*

Michael C. Liu

*Department of Astronomy, University of California, Berkeley,
Campbell Hall, Berkeley, CA 94720, USA*

Stéphane Charlot

*Institut d'Astrophysique du CNRS, 98 bis Boulevard Arago,
75014 Paris, France*

ABSTRACT

We present the first infrared (IR) color-magnitude diagram (CMD) for the halo of a giant elliptical galaxy. The CMD for the stars in the halo of NGC 5128 (Centaurus A) was constructed from HST NICMOS observations of the WFPC2 CHIP-3 field of Soria et al. (1996) to a 50% completeness magnitude limit of $[F160W]=23.8$. This field is located at a distance of $08' 50''$ (~ 9 kpc) south of the center of the galaxy. The luminosity function (LF) shows a marked discontinuity at $[F160W]\approx 20.0$. This is $1 - 2$ mag above the tip of the red giant branch (TRGB) expected for an old population (~ 12 Gyr) at the distance modulus of NGC 5128. We propose that the majority of stars above the TRGB have intermediate ages (~ 2 Gyr), in agreement with the WFPC2 observations of Soria et al. (1996). Five stars with magnitudes brighter than the LF discontinuity are most probably due to Galactic contamination. The weighted average of the mean giant branch color above our 50% completeness limit is $[F110W]-[F160W]=1.22\pm 0.08$ with a dispersion of 0.19 mag. From our artificial-star experiments we determine that the observed spread in color is real, suggesting a real spread in metallicity. We estimate the lower and upper bounds of the stellar metallicity range by comparisons with observations of Galactic star clusters and theoretical isochrones. Assuming an old population, we find that, in the halo field of NGC 5128 we surveyed, stars have metallicities ranging from roughly 1% of solar at the blue end of the color spread to roughly solar at the red end, with a mean of $[Fe/H]=-0.76$ and a dispersion of 0.44 dex.

Subject headings: stars: AGB and post-AGB; galaxies: elliptical and lenticular, cD;
galaxies: evolution; galaxies: formation; galaxies: individual: NGC 5128

1. Introduction

Individual stars are the visible building blocks of galaxies and direct tracers of the galaxy formation process. Massive elliptical galaxies are believed to contain the majority of the oldest stars in the Universe (Tinsley and Gunn 1976). Two main scenarios have been proposed for the formation of these galaxies. In the traditional scenario of single “monolithic” collapse, the most massive early-type (E and S0) galaxies form at early times ($z \gtrsim 2$) and evolve with little or no star formation thereafter (Tinsley 1980; Bruzual and Kron 1980; Koo 1981; Shanks et al. 1984; King and Ellis 1985; Yoshii and Takahara 1988; Guiderdoni and Rocca-Volmerange 1990). In hierarchical models of galaxy formation, massive galaxies assemble later ($z \lesssim 2$) from mergers of smaller subunits (e.g., White and Rees 1978; White and Frenk 1991; Lacey et al. 1993; Kauffmann, White and Guiderdoni 1993; Cole et al. 1994; Somerville 1997). At least some elliptical galaxies show signatures of intermediate-age stars in addition to an old stellar population (e.g., Worthey, Faber and Gonzalez 1992). Dynamical studies also suggest that the pressure support of stellar populations in elliptical galaxies could result from mergers (Toomre and Toomre 1972; Hibbard et al. 1994). Moreover, detailed observations of some elliptical galaxies reveal morphological and kinematic signs of a past merging event. These range from the observations of proto-elliptical merger remnants like NGC 7252 to evidence of counter-rotating or otherwise decoupled cores for nearby ellipticals (star-star or star-gas, Bertola 1997). The dominance of old stars and evidence of merging in elliptical galaxies can be understood simultaneously if the youngest stars contribute only a small fraction of the observed integrated light. In fact, Silva and Bothun (1998) show that nearby elliptical galaxies with morphological signatures of recent merger activity have near-IR colors similar to those of galaxies not showing signs of mergers. They conclude that intermediate-age (1 – 3 Gyr) stars contribute at most 10%–15% of the total stellar mass in galaxies with recent merger activity in their sample.

Resolving individual stars in elliptical galaxies has become feasible only recently with the advent of the Hubble Space Telescope (HST), since no suitable examples are near enough to be observed from the ground (this will change with the application of adaptive optics systems to large ground-based telescopes). Such detailed information about the stellar content of elliptical galaxies can help us reconstruct their star formation history, and hence, constrain their process of formation. With HST, it is possible to resolve the population of the massive elliptical galaxy NGC 5128 (Centaurus A) due to its proximity to us. NGC 5128 is part of a group of 25 galaxies composed mainly of dwarf galaxies extending over about 25 degree on the sky (see review by Israel 1998). Its distance estimate relies upon different measurement methods. A distance modulus of $(m - M)_0 = 27.53 \pm 0.25$ (Tonry and Schechter 1990) is derived from the globular cluster luminosity function (LF) of Harris (1986). The planetary nebula luminosity function yields $(m - M)_0 = 27.73 \pm 0.14$

(Hui et al. 1993). The distance modulus of $(m - M)_0 = 27.48 \pm 0.06$ measured by Tonry and Schechter (1990) from surface brightness fluctuations is revised to $(m - M)_0 = 27.71 \pm 0.10$ by Israel (1998) using the results of Tonry (1991) (the more recent results of Tonry et al. (1997) yield a higher revised value of $(m - M)_0 = 28.18 \pm 0.07$). An estimate of $(m - M)_0 = 27.72 \pm 0.20$ is derived from the magnitude of the tip of the red giant branch (TRGB) for stars in the halo observed with HST WFPC2 by Soria et al. (1996; hereafter SMW96). A more recent measurement by Harris et al. (1999; hereafter HHP99) comes from the magnitude of the TRGB for stars in another halo field observed with HST WFPC2 (these data reach ~ 3 magnitudes down the RGB). They find a distance modulus of $(m - M)_0 = 27.98 \pm 0.15$, or $D = 3.9 \pm 0.3$ Mpc. The weighted average of distance moduli of $(m - M)_0 = 27.75 \pm 0.06$ is adopted throughout this paper and corresponds to a distance of $D = 3.5 \pm 0.1$ Mpc. At this distance, 1 arcmin corresponds to 1018 pc.

NGC 5128 is a clear case of an elliptical galaxy showing signs of past merger activity. It is one of the largest known radio galaxies (500×250 kpc wide) and a massive disk of gas, young stars, and dust is embedded in its center. Within a radius of about $18'$ from the nucleus, the galaxy shows optical shell structures made up of old disk stars and associated H I shells (Schiminovich et al. 1994). This suggests that NGC 5128 might have experienced more than just one merger in its past (Weil and Hernquist 1996). The H I shells detected in the outer part of the galaxy seem to show signs of recent star formation (Graham 1998). The halo globular clusters in NGC 5128 (region in radius $R < 24'$) have a mean metallicity of $[\text{Fe}/\text{H}] = -0.8 \pm 0.2$ (0.5 dex higher than their Milky Way counterparts; Harris et al. 1992) and show a bimodal distribution in color, with peaks at $[\text{Fe}/\text{H}] \simeq -1.1$ and -0.3 ($R > 4'$; Harris et al. 1992), an effect commonly associated with a merging event. Jablonka et al. (1996) find no object with a metallicity higher than solar in a similar sample. The globular clusters in the inner 3 kpc are more metal rich with $-0.6 \leq [\text{Fe}/\text{H}] \leq +0.1$ than in the outer regions and show signs of a metallicity gradient (Jablonka et al. 1996; Minniti et al. 1996; Alonso and Minniti 1997). Recent HST WFPC2 observations yield a mean value of $[\text{Fe}/\text{H}] > -0.9$ (SMW96) and $[\text{Fe}/\text{H}] = -0.41$ (HHP99) for red giant branch stars in the halo of NGC 5128.

The age of the current burst of star formation in the disk of NGC 5128 is typically a few times 10^7 years (van den Bergh 1976; Dufour et al. 1979). In the halo, the presence of ~ 200 stars found to be brighter than the TRGB prompted SMW96 to suggest the presence of an intermediate-age population of ~ 5 Gyr, making up at most 10% in number of the total halo population. Dynamical estimates based on the model of a merger of a late-type galaxy of mass a few times $10^{10} M_\odot$ with NGC 5128 suggest a more recent merging timescale of a few hundred million years (Tubbs 1980; Malin, Quinn and Graham 1983). The total mass of the galaxy estimated from velocity dispersion measurements of the planetary nebula system is $M = 4 \pm 1 \times 10^{11} M_\odot$, with half of it estimated to be due to dark matter (Mathieu, Dejonghe and Hui 1996).

We present in this paper the first IR color-magnitude diagram (CMD) for the halo of a giant elliptical galaxy. Our NICMOS observations of the halo of NGC 5128 probe a range of ~ 4 magnitudes down the luminosity function to our 50% completeness limit. Section 2 presents the details of the NICMOS observations we obtained in August 1998. The data analysis using the stellar

photometry package DAOPHOT is described in Section 3. The importance of doing artificial-stars experiments is emphasized in Section 4, where the completeness functions are presented. The luminosity functions and discontinuities are derived in Section 5. Section 6 presents the first IR CMD of the halo of NGC 5128. This section is divided into four sub-sections discussing the total uncertainties, deriving an estimate of the metallicity spread of the halo stars, and discussing the nature of the bright stars above the TRGB of an old population. A summary of our results and conclusions appears in Section 7. The more technical details of the magnitude system transformations are given in Appendix A.

2. Observations

Images of a field in the halo of NGC 5128 were taken on 1998 August 31 with the NIC1 and NIC2 camera of the Near-Infrared and Multiobject Spectrometer (NICMOS) (Thompson et al. 1998) on board HST. The spacecraft pointing was chosen to image the existing WFPC2 CHIP-3 field of SMW96, at a distance of $08' 50''$ from the nucleus, with the NICMOS cameras (see Figure 1). We chose our positions of NIC1 and NIC2 so they would lie inside the WFPC2 CHIP-3 field of view of SMW96 for any unrestricted value of position angle. Based on our adopted distance of 3.5 Mpc, this corresponds to a distance of ~ 9 kpc south of the center of the galaxy. The geometrical center of NIC2 was at position $\alpha = +13^{\text{h}}25^{\text{m}}24^{\text{s}}.323$, $\delta = -43^{\circ}09' 58''.53$ (J2000) and the NIC1 observations were obtained in parallel. The NIC2 detector has a field of view of $19''.2 \times 19''.2$ with 256 pixels on a side and $0''.075$ per pixel. A total of 8192 s (3 orbits) of integration time were obtained, 5376 s in the F160W filter and 2816 s in the F110W filter. The observations were taken in a four dither positions mode with offsets of (0,0), (0,15.5), (15.5,15.5), and (15.5,0) pixels, corresponding to a maximum shift of $1''.17$. This enables the replacement of a bad pixel in one frame with the average of good pixels from dithered frames. In addition, short exposures were taken at the beginning of each orbit in the MULTIACCUM mode to reduce the cosmic rays persistence effects (Najita, Dickinson and Holfeltz 1998). All the observations were taken in the MULTIACCUM mode with the SPARS64 sequence.

A basic image reduction was done by STScI using the standard NICMOS pipeline procedure called CALNICA which performs bias subtraction, dark-count correction, and flat-fielding (MacKenty et al. 1997). Our own subsequent data reduction with IRAF¹ consisted of masking bad pixels, correcting for a constant level offset between the four quadrants of the NIC2 camera, correcting for background variations by subtracting a median sky image and adding back a constant sky level, and averaging the images. Each resulting NIC2 mosaic covers a field of view of $20''.4 \times 20''.4$. The final combined NIC2-F110W and -F160W images of our field are shown in Figure 2.

¹IRAF is distributed by the National Optical Astronomy Observatories, which are operated by the Association of Universities for Research in Astronomy, Inc., under cooperative agreement with the National Science Foundation.

3. Stellar Photometry

Photometry was obtained for our NICMOS images by using the automated star-detection algorithm DAOPHOT (Stetson 1987, 1992). The data were initially processed using the subroutine DAOFIND with a conservative detection threshold of 5σ above the local background level. The PSFs were derived by using many well-exposed, isolated stars sampling the frame uniformly. The full width at half-maximum (FWHM) of the F160W and F110W PSF profiles were measured to be equal to 1.7 and 1.2 pixel, respectively. The stellar photometry was accomplished by processing our images using the subroutine ALLSTAR once, and then another time on the first residual image. The fitting was done on pixels within a fitting radius of the centroid of a star equal to the FWHM of the PSF. The 3-parameter least-square fit to the star determines the position of the center (x,y), the brightness and its standard deviation. We measured magnitudes for 971 stars in the F110W image and 1321 stars in the F160W image.

The residual images generated by DAOPHOT show that stars near the edges of the mosaics suffer from bad PSF fits (their distance from the edge is of the order of their FWHM). Our final sample contains stars selected so that they are not too close to the edge of the mosaic, i.e., no less than 3 pixels away from the edge. We also applied a stellar fit χ^2 cut to our sample of stars. The cut was set to a χ^2 of 2.6, given that the probability of exceeding that value of χ^2 is 5%. The χ^2 test was done only on the F160W image for which the PSF is well sampled. In the case of the under-sampled F110W image for which the PSF is almost a Dirac delta function, χ^2 provides a poor discriminant because it is possible to fit every pixel that contains a signal. The [F160W] χ^2 cut eliminated 215 stars of which 3 were on the right hand side of the red envelope of the normal giants in our CMD, leaving a single extremely red star at [F110W]–[F160W]= 2.5 ± 0.1 (see Section 6 and Figure 7).

The instrumental magnitudes were transformed into the Vega-based system. Since the photometric keywords needed to transform countrates into magnitudes refer to a nominal infinite aperture, given in the HST Data Handbook as 1.15 times the flux in a 0.5 arcsec radius aperture, the measured countrates have to be corrected accordingly. This is done by first correcting the measured PSF-fitting photometry to the 0''.13 radius aperture photometry (a 0''.13 or 1.7 pixel radius aperture, of the order of the FWHM of the F160W PSF, was used to calibrate the PSF flux in both filters). Secondly, in order to estimate the aperture correction, we used both our observed PSF and the artificial PSF generated by the Space Telescope package TINYTIM (Krist 1993). We found for our choice of aperture radius of 0''.13 that the fraction of PSF-fitting photometry to 0''.5 radius aperture was 60% for the F110W filter and 56% for the F160W filter. Putting in the final 1.15 correction factor, we calculated a correction to brighter magnitudes of 0.71 and 0.77, respectively. The photometric calibration of $\text{PHOTFNU} = 2.190 \times 10^{-6}$ Jy sec/DN and $\text{ZP(Vega)} = 1083$ Jy (HST Data Handbook; updated values from Rieke 1999) produced the NIC2-F160W zeropoint in the Vega-based system of 21.74. After including the aperture correction, the Vega-based magnitudes for stars in our F160W image were therefore computed by using $\text{mag (Vega-based)} = 20.97 - 2.5\log(\text{counts(e-/s)})$ (gain is 5.0 e-/DN). The F110W zeropoint was calculated

to be 21.64, given $\text{PHOTFNU} = 2.031 \times 10^{-6}$ Jy sec/DN, $\text{ZP(Vega)} = 1775$ Jy and the aperture correction given above. The systematic errors in magnitude and color measurements are estimated to be less than 0.05 mag (Calzetti et al. 1999; see Colina and Rieke 1997 for more detail).

Colors were calculated for the stars in the NICMOS images in the following way. Each color image was analyzed separately. The identification of a star in both images was done by requesting that (1) the two positions agreed to a specific tolerance (matching) radius, and (2) the star assigned was the closest uniquely assigned star in either color image. A total of 666 stars (out of the sample of 1087 stars in F160W and 941 stars in F110W) were identified in both filters using a maximum matching radius $r_m = 1$ pixel. This maximum matching radius was chosen because the number of stars matched show a clear cut at that radius, as seen in Figure 3 where we allowed the matching radius to be as large as $r_m = 5$ pixels.

To justify our choice of the maximum matching radius and illustrate that the peak of the distribution lies between 0.1 – 0.2 pixel, we modeled the number of stars with a match between the F110W and F160W images. The model is made up of a Gaussian component that reflects the uncertainty in the centroid of each image, due to undersampling in the F110W image, photon statistics, and the effects of crowding. To this we add a constant background probability of making a false match with an un-associated star. Hence the number of stars matching, N , between radii r and $r + dr$ should follow:

$$N(r) dr = N_{true} \left(\frac{r}{\sigma^2} \right) e^{-0.5(\frac{r}{\sigma})^2} dr + 2 \pi r N_* dr,$$

where N_{true} is the number of true matches, N_* is the number of un-associated stars per unit area, and σ represents the two-dimensional relative error in star positions between the two frames. The best fit curve is shown over-plotted on the histogram of matching radius in Figure 3. This implies that the net two-dimensional root-mean-square (rms) registration error between the F110W and F160W frames is 0.19 pixel, and that a natural choice of cut-off is at a radius of 1 pixel which is equivalent to 5σ . The excess matches above the fit between radii of 0.6 – 0.9 pixels is due to genuine matches of faint stars with poorly determined centroids. The false match rate implies that within our chosen cutoff of 1 pixel, 3% of our stars are matched with the wrong counterpart.

4. Artificial-Star Tests

In the absence of other systematic errors, the photometric errors depend only on photon statistics (from source and background) and detector noise. Simulations we ran prior to our observations showed that in order to be limited by these errors and not be affected by crowding, we needed to observe a region with a surface brightness no higher than 21.0 mag/arcsec² in the F160W filter (assuming a Baade’s window LF). This is consistent with analytic estimates of the effects of crowding (Renzini 1998). In the simulations, we were able to recover the input luminosity function down to

$[F160W] \simeq 23.5$ with photometric accuracy to the 10% level. To assess the errors associated with doing photometry in our field, we simulated artificial stars in our NICMOS images.

TABLE 1
COMPLETENESS

Magnitude	Completeness (%) [F110W]	Completeness (%) [F160W]
20.0	100	100
20.5	100	99
21.0	100	98
21.5	98	98
22.0	99	98
22.5	98	98
23.0	98	94
23.5	95	78
24.0	87	33
24.5	52	5
25.0	17	3
25.5	4	2
26.0	2	2
26.5	2	2

Completeness tests were performed by adding artificial stars to each individual color image. We simulated stars with F110W and F160W magnitudes between 20.0 and 26.5, at a 0.1 mag interval. Each simulation consisted of adding 132 stars to the real image, corresponding to 10% in number of the stars recovered from the F160W image. The number of artificial stars was chosen to be large enough to compile accurate statistics on incompleteness and photometric errors, and small enough to increase the crowding negligibly. The positions of the added stars on the images were randomly chosen but identical for both the F110W and F160W images so that colors could be measured. The frames were then processed in a manner identical to the original data. The F110W and F160W completeness functions measured from these artificial-star tests are shown in Figure 4 and listed in Table 1. The 50% completeness level occurs at $[F110W]=24.5$ and $[F160W]=23.8$, respectively.

5. The Luminosity Functions

Our NICMOS observations probe ~ 4 magnitudes below the tip of the luminosity function down to our 50% completeness limit. The NICMOS data are less crowded by bright stars than the WFPC2 data since the IR luminosity functions tend to be steeper and so there are fewer bright

stars. Figure 5 shows the luminosity functions for stars detected in the F110W and F160W image respectively, taking into account the edge and χ^2 cuts. Also shown in Figure 5 and listed in Table 2 are the luminosity functions for each respective color image obtained after applying the matching criterion ($r_m = 1$ pixel). The red F160W stars that were not matched/detected in the F110W image contribute to the F160W LF only at faint magnitudes ($[F160W] \gtrsim 22.0$).

The matched F160W LF displayed in Figure 5 clearly shows a discontinuity in the number of stars at $[F160W] \approx 20.0$. Although no other clear discontinuity is visible at fainter magnitudes, the slope of the counts changes slightly at $[F160W] \approx 21.0$. As will be discussed in detail in Section 6, these discontinuities are thought to be associated with the TRGB of an intermediate-age and old population in the halo of NGC 5128. In the IR, the presence of an intermediate-age population and an old population will be blended and make the TRGB of the old population difficult to detect while the younger population will be clearly brighter and more visible. Note that the stars brighter than the $[F160W] \approx 20.0$ discontinuity are most probably due to Galactic contamination (see Section 6.3 for discussion).

Given that no IR surface brightness measurements for the halo of NGC 5128 can be found in the literature, it is only possible to estimate this based on the V-band measurements of van den Bergh (1976). The V-band surface brightness at the radial distance of our field is measured to be $23.2 \text{ mag/arcsec}^2$. This corresponds to a $[F160W]$ surface brightness value of $20.2 \pm 0.1 \text{ mag/arcsec}^2$, assuming the color transformation $V - H = 3.1 \pm 0.1$ (Persson, Frogel and Aaronson 1979) and using the magnitude system transformations given in Appendix A. This mean color and standard deviation are calculated based on the distribution in $V - H$ of the Persson, Frogel and Aaronson (1979) field ellipticals. The total light in our resolved population that passes the edge and χ^2 cuts averages to $21.3 \text{ mag/arcsec}^2$. Hence, $\sim 40\%$ of the light is resolved into the stars appearing in the $[F160W]$ LF (see Figure 5; top panel). This result is consistent with a Baade’s window luminosity function (used in our simulations) and confirms that we are not confused by crowding for $[F160W] \lesssim 23.5$.

6. IR Color Dispersion

The NICMOS CMD for NGC 5128 is shown in Figure 7. An electronic version of the photometry table may be obtained on request from the first author. The foreground reddening in the direction of our NICMOS field is $E(B - V) = 0.11 \pm 0.02$ (Frogel 1984; Harris et al. 1992). For $R_V = 3.1$, this corresponds to $A_J = 0.10$, $A_H = 0.06$ and $E(J - H) = 0.04$ (Rieke and Lebofsky 1985). Also shown in this figure is the mean color and standard deviation measured at each magnitude bin. The color histograms and Gaussian fits from which these means and standard deviations were computed are shown in Figure 8. The reader is referred to Table 2 for the list of statistical measurements computed for the real data as well as for the artificial-stars tests. The weighted average of the mean giant branch color above our 50% completeness limit is $[F110W] - [F160W] = 1.22 \pm 0.08$ ($(J - H)_{CIT} = 0.78$) with a dispersion of 0.19 mag.

6.1. Discussion of Uncertainties

In order to estimate the metallicity spread in our IR-selected sample of halo stars, we first need to check whether the spread in color we detect in our data is real. We can then use the Bruzual and Charlot (2000; hereafter BC00) isochrones, described in detail in Section 6.2, to estimate the metallicity spread associated with the observed real color spread.

We begin by comparing the observed spread with the total uncertainties (statistical+systematic errors) calculated from the artificial-star tests. The error in color cannot simply be measured by adding in quadrature the uncertainty in $[F110W]$ and $[F160W]$ because the covariance of these errors is not zero; i.e., the errors are correlated. This occurs because the photometric errors are not random but associated with systematic errors that occur in the photometry of crowded fields; faint stars next to brighter ones will have correlated errors in their $F160W$ and $F110W$ photometry. The photometric errors for the $[F160W]$ magnitudes do not appear in Figure 7 as they are smaller than the symbols used to plot the points. The mean of the DAOPHOT $[F160W]$ photometric errors for our artificial-star tests are added up in quadrature and listed in Table 2. The artificial-star tests total uncertainty measurements become larger than the DAOPHOT photometric errors only in the faintest magnitude bin where the systematic errors (mostly due to crowding of faint stars) become dominant.

The standard deviations in mean color for the seven magnitude bins, as listed in Table 2 and shown in Figure 7, can be compared with the total uncertainties measured from the artificial-stars tests. The observed spread is larger than the total uncertainty in all bins except the faintest one near our 50% completeness limit. For the faintest magnitude bin, we are only 0.3–0.8 magnitude above our 50% completeness limit. For the three brightest bins, the observed spread is larger than the total uncertainty by at least a factor of 1.5–3.5. Assuming that the total uncertainty and intrinsic color spread add in quadrature, the observed rms for the magnitude bin $[F160W]=22.0\text{--}22.5$ of 0.20 ± 0.02 mag implies a *real* color spread of 0.11 ± 0.02 mag. We find for the 12 Gyr isochrones of BC00 (see Section 6.2) that at $M_{[F160W]} = -5.5$:

$$\frac{d[Fe/H]}{d([F160W] - [F110W])} = 2.03 \text{ dex/mag}.$$

This means that a 0.1 mag error in color corresponds to a 0.2 dex error in metallicity. Hence, the real color spread of 0.11 ± 0.02 mag corresponds to a rms for $[Fe/H]$ of 0.22 ± 0.04 dex. The FWHM of the metallicity distribution is then 0.5 ± 0.1 dex.

TABLE 2
LUMINOSITY FUNCTIONS AND COMPARISON BETWEEN
OBSERVED $[F110W]\text{--}[F160W]$ COLOR SPREAD AND TOTAL UNCERTAINTY

[F160W] mag bin	N_{F160W} ($\chi^2 \leq 2.6$)	Observed mean color	Observed rms color	Artificial mean color	Artificial rms color	DAOPHOT rms color error	N_{F110W}
17.0–17.5	1		0
17.5–18.0	0		1
18.0–18.5	0		0
18.5–19.0	1		0
19.0–19.5	2		0
19.5–20.0	1		1
20.0–20.5	6		2
20.5–21.0	24	1.25	0.17±0.02	1.3	0.05	0.10	1
21.0–21.5	39	1.24	0.14±0.02	1.3	0.06	0.11	1
21.5–22.0	95	1.27	0.18±0.02	1.3	0.11	0.11	20
22.0–22.5	163	1.24	0.20±0.02	1.2	0.17	0.13	37
22.5–23.0	165	1.18	0.23±0.01	1.2	0.17	0.15	59
23.0–23.5	129	1.05	0.24±0.02	1.0	0.24	0.19	150
23.5–24.0	36	0.77	0.20±0.08	0.8	0.29	0.22	212
24.0–24.5	4		201
24.5–25.0	0		52
25.0–25.5	0		2

6.2. Estimate of the Metallicity Spread

We now compare our IR CMD with the observed cluster giant branches and theoretical isochrones from Bertelli et al. (1994) and BC00 to estimate the upper and lower bound on the metallicity distribution of the stars in the halo of NGC 5128.

We compare our data with the red giant branches of the clusters M92, 47 Tuc, M67, and NGC 6553 in Figure 9. The references for the cluster data, their distance moduli, and their metallicities are listed in Table 3. The star cluster magnitudes were transformed to [F160W] and [F110W] magnitudes according to the formulae given in Appendix A. The NGC 6553 giant branch of Davidge and Simons (1994) was corrected for reddening ($E(J - H) = 0.231$) and extinction ($A_H = 0.38$) (Rieke and Lebofsky 1985; Guarnieri et al. 1998). The metallicity bounds on the data are chosen to bracket $\pm 1\sigma$ of the real color spread. The most metal poor stars in this halo field have metallicities matching those of the globular cluster M92 with $[\text{Fe}/\text{H}] = -2.03$. This is in good agreement with the lower metallicity bound derived by SMW96 and HHP99. At the other end of the metallicity range NGC 6553, with $[\text{Fe}/\text{H}] = -0.29$, reproduces well the upper bound of our IR data as for the optical data of HHP99. The cluster M67 is consistent with being more metal rich than 47 Tuc but its low magnitude giant branch restricts us from using it as a comparison to our data. From this comparison we conclude that the metallicity spread based on the color spread in the IR halo data is $-2.0 \lesssim [\text{Fe}/\text{H}] \lesssim -0.3$ (these limits cover slightly more than $\pm 1\sigma$ of the real color

spread; see Figure 9). This comparison confirms the presence of a metallicity spread as estimated in Section 6.1.

Assuming an old population, the IR data support the findings of SMW96 and HHP99 in the optical suggesting that the halo of NGC 5128 is composed of stars ranging from metal-poor to near-solar metallicities. To complicate things, the presence of an intermediate-age population, as will be discussed in Section 6.4, can be another contributor to the large spread in metallicities at magnitudes below the TRGB where the populations become intertwined. In fact, it is worth noting that previous work, including the analysis presented here, has not solved for the age of the population but assumed it to be old in order to solve for the metallicity spread. If we assume that the spread in metallicity is indeed associated with an old population, then this spread suggests that metal enrichment occurred during the primordial collapse of the galaxy, or alternative, that a low-metallicity component was accreted from an external source. Based on the hierarchical picture of galaxy formation, HHP99 proposed that the old metal-poor stars in the halo formed during a first burst of star formation occurring in the in-falling clumps of gas. A first wave of supernovae explosions then ejected and enriched the gas that eventually fell back into the potential well ($\sim 1-2$ Gyr later) to form the more metal-rich stars in the halo.

The comparison with star cluster data is the best evidence of a spread in metallicity in the old population of NGC 5128. Because of the model uncertainties, comparison with theoretical isochrones can only be used as an example of how to tie the spread in colors to a spread in absolute metallicity. We compare our data with the 12 Gyr old stellar population isochrones of Bertelli et al. (1994) in Figure 10. For a meaningful comparison, the magnitudes were properly transformed using the mathematical expressions derived in Appendix A. The isochrones shown in Figure 10 are for the metallicities $[\text{Fe}/\text{H}] = -1.7, -0.7, -0.4, +0.0$, and $+0.4$. The upper parts of these IR isochrones with $[\text{Fe}/\text{H}] \geq -1.7$ (e.g., $[\text{F160W}] < 22.19$ or $M_{H_{BB}} < -5.59$ for $[\text{Fe}/\text{H}] = -0.7$; BB refers to the Bessell and Brett (1988) system; see Appendix A and Figure 6) are not yet satisfactory according to Bertelli (1999), due to the problems in atmosphere models and scales of effective temperature for M giants. The comparison shows that our data are clearly more metal rich than the $[\text{Fe}/\text{H}] = -1.7$ isochrone and at least as metal rich as $[\text{Fe}/\text{H}] = -0.7$. Unfortunately, we cannot put a stronger upper limit on the spread in metallicity because of the problems described above.

We also make use of the most up-to-date stellar evolution models of BC00 to interpret the color spread in our CMD. The new isochrones of BC00 are generated from the new library of metallicity-dependent spectra calibrated by Lejeune, Cuisinier and Buser (1997, 1998) and an improved color-effective temperature relation for cool stars. In addition, the BC00 isochrones include the carbon AGB stars (see BC00 and Liu, Charlot and Graham 2000 for details). The prescriptions for those are semi-empirical, and essentially based on models and observations of stars in the Small Magellanic Cloud (SMC), Large Magellanic Cloud (LMC), and Milky Way. The BC00 isochrones indicate more clearly a mean metallicity of $[\text{Fe}/\text{H}] \sim -0.4$ to -0.7 , depending on magnitude (see Figure 8), and a range of $-1.7 \lesssim [\text{Fe}/\text{H}] \lesssim +0.0$, where the lower limit is clearly too low for the $\pm 1\sigma$ color spread. The theoretical isochrones indicate a slightly more metal-rich spread

in metallicities than the estimate from cluster giant branches. This is also observed in the optical data of HHP99. The red upper limit indicates that the most metal rich stars in the halo field we observed with NICMOS are roughly solar in metallicity.

We use the 12 Gyr isochrones of BC00 to estimate the metallicity for individual stars in our NICMOS field. The metallicity histogram is therefore only derived for stars with $[\text{Fe}/\text{H}] = -1.7$ to $+0.4$. The histogram shown in Figure 11 for each 0.5 magnitude bin in the range $[\text{F160W}] = 21.0 - 24.0$ was generated for stars which fell on or in between isochrones and for which we could estimate the metallicity by using a simple linear interpolation method. This is a very crude and model dependent estimate of the metallicity, as it does not include stars above the 12 Gyr isochrone TRGBs (e.g., bright intermediate-age AGB stars) and ignores the stars redder (e.g., post-AGB stars in their superwind phase) and bluer than the predicted colors (see Figure 11). The metallicity distribution for a total of 353 stars in our CMD, shown in Figure 12, peaks at $[\text{Fe}/\text{H}] = -0.76$ with a dispersion of $\sigma = 0.44$. This peak and dispersion agree well with the overall metallicity distribution of the globular clusters and of the halo stars of HHP99 (see Figure 12; Harris et al. 1992; HHP99). The $[\text{Fe}/\text{H}]$ distribution of stars in our NICMOS field does not seem to be resolved into multiple peaks, as is the case for the halo stars of HHP99. We find no obvious sign of a “sub-peak” which would match the largest sub-peak of the halo metallicity distribution of HHP99 at $[\text{Fe}/\text{H}] = -0.32$ with a dispersion of $\sigma = 0.22$, corresponding nicely with the second largest sub-peak in the globular cluster metallicity distribution. It is not clear at this point if the difference in the shape and peak of the metallicity distribution between the IR and the optical data of HHP99 is real or due to the large uncertainty associated with the color-metallicity transformation. The general agreement of the metallicity spread is promising; the combination of the NICMOS observations and the F555W and F814W observations of SMW96 of the same halo field should help resolve the issue (Marleau et al. 2000).

TABLE 3
ADOPTED PARAMETERS FOR M92, 47 TUC, M67, AND NGC 6553

Star Cluster	Cluster Type	CMD Data	$[\text{Fe}/\text{H}]$	$(m - M)_0$	Magnitude System	References
M92	Globular	4	-2.03	14.6	CIT	1
47 Tuc	Globular	7	-0.65	13.4	CIT	2
M67	Old Open	3	-0.09	9.38	CIT	3,4
NGC 6553	Globular	5	-0.29	13.6	CIT	5,6

NOTES TO TABLE 3

- (1) Stetson and Harris (1988); (2) Hesser et al. (1987); (3) Houdashelt, Frogel and Cohen (1992); (4) Cohen, Frogel and Persson (1978); (5) Davidge and Simons (1994); (6) Guarnieri, Renzini and Ortolani (1994); (7) Frogel, Persson and Cohen (1981)

6.3. Bright Stars

As can be seen in Figure 9 and Table 2, we detect a population of bright stars above the TRGB of globular clusters and old stellar populations. These bright stars in our CMD can be due to (1) blended images, (2) Galactic contamination, or (3) a young or intermediate-age halo population.

We searched for blended doubles by first examining the *SHARPNESS* parameter calculated by DAOPHOT. The *SHARPNESS* is defined so that is zero for stars, larger than zero for galaxies or unrecognized blended doubles, and less than zero for cosmic rays or single pixel defects. We plotted the *SHARPNESS* and χ^2 as a function of magnitude for our data and found the *SHARPNESS* parameter to be close to zero for those bright stars above the TRGB, with good values of χ^2 (as expected from our initial χ^2 cut). Therefore, we found no reason to reject them.

The five brightest, blue stars in the upper left region of Figure 13 with $[F160W] < 20.0$ and $0.40 < [F110W] - [F160W] < 0.85$, have colors and magnitudes that are consistent with foreground Galactic stars. The theoretical isochrone of Bertelli et al. (1994) for a 5 Gyr disk population with solar metallicity is shown in Figure 13 assuming a distance modulus for the Galactic stars of 15.0. Main sequence K–M dwarfs have $0.4 \leq J - H \leq 0.7$ (Tokunaga 1995; Davidge 1998) and therefore the five bright stars have colors and magnitudes consistent with K–M dwarfs in our Galaxy. To assess the number of foreground Galactic stars expected to contaminate our data, we used the Galaxy model of Cohen (1993) for IR star counts for the direction $(l, b) = (309.5^\circ, 19.4^\circ)$, adopting a solar displacement of 15 pc, and a halo scale factor of 0.5 (Cohen 1995). Table 4 lists the predicted number of stars for 1 magnitude wide bins for the $[F160W]$ filter. The expected number of foreground stars contaminating each magnitude bin in the F160W image based on Cohen’s model, scaled by a factor of 3.9, is shown in Figure 5. No correction was made between H and $[F160W]$.

TABLE 4
PREDICTED NUMBER OF GALACTIC STARS

$[F160W]$	N_p	$N_p \times 3.9$	N_{obs}
17.0–18.0	0.30	1.17	1
18.0–19.0	0.42	1.64	1
19.0–20.0	0.55	2.14	3
20.0–21.0	0.68	2.65	30
21.0–22.0	0.78	3.04	134
22.0–23.0	0.81	3.16	328
23.0–24.0	0.74	2.89	165
24.0–25.0	0.60	2.34	4
25.0–26.0	0.43	1.68	0
26.0–27.0	0.28	1.09	0

Since the bright stars ($[F160W] < 20.0$) in the NIC2 image have colors consistent with Galactic dwarfs, it seems likely that Cohen model under-predicts the contamination since it predicts only

1.27 stars in the range $[F160W]=17.0-20.0$. The Cohen model has not been validated at these faint magnitudes and therefore we feel justified in applying an arbitrary scaling to the Cohen predictions. A maximum-likelihood analysis shows that scaling up the predicted counts (N_p) by a factor of 3.9 produces the best fit to the observed counts (N_{obs}) with a 95% confidence interval of 2.1 – 8.3. With this scale factor we predict the contamination in fainter magnitude bins as given in Table 4. Clearly, this implies that Galactic contamination is insignificant for all bins fainter than $[F160W]=20.0$.

6.4. The Intermediate-Age Population

The presence of an intermediate-age population of ~ 5 Gyr in the halo of NGC 5128 was proposed by SMW96 based on their detection of ~ 200 stars brighter than the TRGB. We look for the presence of intermediate-age stars as postulated by SMW96 by comparing the IR data with the 2 Gyr old isochrone from BC00 with metallicity $[Fe/H]=-1.7, -0.7, -0.4, +0.0$, and $+0.4$, which include the carbon AGB stars. Figure 13 shows that the presence of an intermediate-age population would be revealed by asymptotic giant branch (AGB) stars ~ 1 mag above the TRGB. This effect is also demonstrated by moving the LMC and SMC AGB stars with ages between 1 – 3 Gyr and the younger stars with ages between 40 – 120 Myr to the distance of NGC 5128 (Frogel et al. 1990). The AGB is composed of M-type (oxygen-rich) stars and, for young- and intermediate-age populations, of C-type (carbon-rich) stars which occupy the bright end of the AGB.

As Figure 13 shows, the LMC and SMC AGB stars belonging to an intermediate-age population occupy a part of the CMD that is also occupied by the brightest IR stars in the halo of NGC 5128. We find that $\sim 10\%$ of the stars resolved in our NICMOS images and appearing in our CMD are brighter than the TRGB of a 12 Gyr old population, assuming a metallicity of $[Fe/H]=+0.0$ (this brightest isochrone TRGB terminates at $[F160W]=21.2$ or $M_{H_{BB}} = -6.6$; BC00). The IR data suggest the presence of an intermediate-age population, also seen in the WFPC2 observations of SMW96. A preliminary match between the IR and the SMW96 optical data shows that our intermediate-age population consists of the same stars that make up the intermediate-age population of SMW96 (Marleau et al. 2000). For their WFPC2 field, located $18'.32$ south of the galaxy center, HHP99 claim that the halo is composed almost entirely of old stars (at most 300 stars, representing $\sim 3\%$ of their sample, belong to an intermediate-age population). As the fraction of intermediate-age stars detected in the WFPC2 SMW96 field, in agreement with our NICMOS field, is larger by at least a factor of ~ 3 at half the radial distance from the galaxy center, it is suggestive of a radial gradient in the stellar population in the halo (the younger population being more centrally concentrated). With the limited area of our NICMOS field and hence the small number statistics, it is not possible to accurately estimate the metallicity mean and spread associated with the intermediate-age population only. Assuming an old halo population, the double metallicity peak in the globular cluster systems of NGC 5128 (Harris et al. 1992) and the halo stars in the HPP99 field at $[Fe/H] \simeq -1.1$ (barely noticeable for the halo stars) and -0.3 is well within

our estimated range in metallicities.

If one excludes the brightest star at $[F160W]=17.15$ which is most certainly due to Galactic contamination, the colors and magnitudes of the other four stars with $[F160W] < 20.0$ are close to being consistent with a very young (40 – 120 Myr) population (see Figure 13). But since their colors are closer to the late type K–M dwarfs which dominate Galactic contamination, we conclude that there is no strong evidence for a very young population of stars in our halo field.

7. Conclusion

We have presented the first IR CMD for the halo of a giant elliptical galaxy. Assuming a distance to NGC 5128 of 3.5 Mpc, we have detected a discontinuity in the luminosity function at $[F160W]\approx 20.0$ and have measured IR magnitudes and colors for stars in the halo of NGC 5128 to $[F160W]=23.8$ (50% completeness limit). We are confident that we are not confused by crowding to $[F160W]\simeq 23.5$ based on careful analysis of artificial-stars tests. The weighted average of the mean color of our giant branch above our 50% completeness limit is $[F110W]-[F160W]=1.22\pm 0.08$ ($(J-H)_{CIT} = 0.78$) with a dispersion of 0.19 mag. From our artificial-star experiments we have determined that there is a real spread in color in our CMD. By comparing our data with star cluster giant branches and theoretical isochrones, we were able to constrain the metallicity spread associated with this real color spread. Assuming an old population, we find that, in the halo field of NGC 5128 we surveyed, stars have metallicities ranging from roughly 1% of solar at the blue end of the color spread to roughly solar at the red end, with a mean of $[Fe/H]=-0.76$ and a dispersion of 0.44 dex.

We assert that the five brightest stars above the SMW96 determination of the TRGB are most probably due to Galactic contamination. We found that the majority of stars above the TRGB of an old population belong to an intermediate-age population (~ 2 Gyr). The presence of an intermediate-age population in the halo of NGC 5128 is consistent with the findings of SMW96. We conclude from our analysis that the IR data are consistent with the halo of NGC 5128 being composed of at least two age populations, a population with ages ~ 2 Gyr and an old population. Assuming an old population, we find that the stars have a wide range of metallicities. Future work will combine the WFPC2 CHIP-3 observations of SMW96 and our NICMOS data to examine the multi-color (F555W, F814W, F110W, and F160W) properties of stars in the halo of NGC 5128 and try to reconstruct the galaxy’s formation history.

F.R.M. would like to thank Nial Tanvir for providing some of the software for the completeness tests and Rachel Johnson for her instructions on aperture photometry corrections. Many thanks to Jay Anderson for the use of his code with which he initially derived for us the WFPC2(SMW96) and NICMOS star matching. We are grateful to Joan Najita and Patricia Royle for private communications while dealing with cosmic rays persistence effects and data reduction related issues.

Finally, we would like to mention that Martin Cohen kindly provided us with the star count calculations from his model. This research was supported by the HST NASA grant STScI GO-07852.02-96A. F.R.M. acknowledges an IoA observational astronomy rolling grant from PPARC, ref. no. PPA/G/O/1997/00793.

A. Magnitude System Transformations

The filters used for the NICMOS observations differ substantially from ground-based IR systems. The central wavelength of F110W is close to that of J -band ($1.3 \mu\text{m}$), but this filter is almost twice as wide as J and transmits from $0.8 - 1.4 \mu\text{m}$. The F160W is analogous to ground-based H , but extends an additional $0.1 \mu\text{m}$ blueward. To facilitate comparison of our NICMOS data with previous ground-based IR observations, and with theoretical isochrones, we have derived color transformations between F110W and F160W and their closest ground-based counterparts, J and H .

We need to compare our data with stellar cluster photometry (all of which is on the CIT system) and with the isochrones of Bertelli et al. (1994) which are presented on the homogenized system proposed by Bessell and Brett (1988). They present an empirical transformation from CIT to their system equal to:

$$(J - H)_{BB} = 0.002 + 1.098 (J - H)_{CIT}.$$

Therefore, we concentrate on calculating the transformation between the BB and NICMOS system. This transformation must be deduced theoretically because only a small number of calibration stars (five) were observed both by NICMOS (see NICMOS calibration web page at STScI) and from the ground (Persson, Frogel and Aaronson 1979). Eventually, when more NICMOS data become public it will be possible to replace this theoretical transformation with an empirical one.

We have calculated synthetic magnitudes for stars in the Pickles (1998) spectral library in the NICMOS and BB systems. Since we have adopted a Vega-based system all colors are relative to that of an A0V star, i.e., if η_λ is the system efficiency, taken from Bessell and Brett (1988) and from the HST Data Handbook version 3.1 March 1998 respectively, and f_λ is the stellar flux, the corresponding synthetic magnitude m_λ is:

$$m_\lambda = -2.5 \log \left(\frac{\int_0^\infty f_\lambda \eta_\lambda d\lambda}{\int_0^\infty f(A0V)_\lambda \eta_\lambda d\lambda} \right).$$

Figure 6 shows an example of synthetic Vega-based colors for the Pickles library stars on the BB and NICMOS systems. The spectral types of the giants are O8III to M10III and O5V to M6V for dwarfs; both normal, and a few metal-poor and metal-rich stars have been included. This figure

shows that there is a significant color difference between $[F110W] - [F160W]$ and $(J - H)_{BB}$. A simple linear fit,

$$[F110W] - [F160W] = -0.058 + 1.484(J - H)_{BB},$$

and

$$[F160W] = 0.019 + 0.095(J - H)_{BB} + H_{BB},$$

describes the transformation accurately. There is some scatter about the straight line for the latest M giants. Given the mean colors of the stars in NGC 5128 we expect any systematic error to be less than 0.1 mag in locating the transformed isochrones. An error of 0.1 mag in $[F110W] - [F160W]$ corresponds to a 0.2 dex error in metallicity.

The colors for five stars observed as part of the NICMOS photometric calibration campaign with magnitudes measured in both the NICMOS and Las Campanas Observatory (LCO) (Persson, Frogel and Aaronson 1979) systems are also plotted in Figure 6. The LCO magnitudes of these stars were first transformed to the BB system. Comparison of the data with the synthetic photometry in Figure 6 confirms that the theoretical colors are satisfactory and that the transformation can be made reliably for normal stars. Some of Persson’s stars are highly reddened and fall off the linear trend. However, nearly all of our stars have $[F110W] - [F160W] < 1.5$, and so the quadratic term that emerges for very red stars is not relevant.

REFERENCES

- Alonso, M.V., and Minniti, D. 1997, *ApJS*, 109, 397
- Bertelli, G. 1999, private communication
- Bertelli, G., Bressan, A., Chiosi, C., Fagotto, F., and Nasi, E. 1994, *A&A*, 106, 275
- Bessell, M.S., and Brett, J.M. 1988, *PASP*, 100, 1134
- Bruzual, A.G., and Charlot, S. 2000, in preparation (BC00)
- Bruzual, A.G., and Kron, R.G. 1980, *ApJ*, 241, 25
- Calzetti, D., Dickinson, M., and Rieke, M. 1999, private communication
- Cohen, M. 1995, *ApJ*, 444, 874
- Cohen, M. 1993, *AJ*, 105, 1860
- Cohen, J.G., Frogel, J.A., and Persson, S.E. 1978, *ApJ*, 222, 165

- Cole, S., Aragón-Salamanca, A., Frenk, C.S., Navarro, J.F., and Zepf, S.E. 1994, MNRAS, 271, 781
- Colina, L., and Rieke, M.J. 1997, in *HST Calibration Workshop*, eds. S. Casertano et al.
- Davidge, T.J. 1998, ApJ, 497, 650
- Davidge, T.J., and Simons, D.A. 1994, AJ, 107, 240
- Dufour, R.J., van den Bergh, S., Harvel, C.A., et al. 1979, ApJ, 84, 284
- Frogel, J.A., Terndrup, D.M., Blanco, V.M., and Whitford, A.E. 1990, ApJ, 353, 494
- Frogel, J.A. 1984, ApJ, 278, 119
- Frogel, J.A., Persson, S.E., and Cohen, J.G. 1981, ApJ, 246, 842
- Graham, J. A. 1998, ApJ, 502, 245
- Guarnieri, M.D., Ortolani, S., Montegriffo, P., Renzini, A., Barbuy, B., Bica, E., and Moneti, A. 1998, A&A, 331, 70
- Guarnieri, M.D., Renzini, A., and Ortolani, S. 1997, ApJ, 477, L21
- Guiderdoni, B., and Rocca-Volmerange, B. 1990, A&A, 227, 362
- Harris, G.L.H., Harris, W.E., and Poole, G.B. 1999, AJ, 117, 855 (HHP99)
- Harris, G.L.H., Geisler, D., Harris, H.C., and Hesser, J.E. 1992, AJ, 104, 613
- Harris, W.E. 1986, in The Harlow Shapley Symposium on Globular Cluster Systems in Galaxies, IAU Symposium No. 126, edited by J.E. Grindlay and A.G.D. Philip (Reidel, Dordrecht), p. 237
- Hesser, J.E., Harris, W.E., VandenBerg, D.A., Allwright, J.W.B., Shott, P., and Stetson, P.B. 1987, PASP, 99, 739
- Hibbard, J.E., Guhathakurta, P., van Gorkom, J.H., and Schweizer, F. 1994, AJ, 107, 67
- Houdashelt, M.L., Frogel, J.A., and Cohen, J.G. 1992, AJ, 103, 163
- Hui, X., Ford, H.C., Ciardullo, R., and Jacoby, G.H. 1993a, ApJ, 414, 463
- Israel, F.P. 1998, A&A Rev., 8, 237
- Jablonka, P., Bica, E., Pelat, D., and Alloin, D. 1996, A&A, 307, 385
- Kauffmann, G., White, S.D.M., and Guiderdoni, B. 1993, MNRAS, 264, 201
- King, C.R., and Ellis, R.S. 1985, ApJ, 288, 456

- Koo, D.C. 1981, PhD thesis, University of California at Berkeley
- Krist, J. 1993, in *Astronomical Data Analysis Software and Systems II*, 52, eds. R.J. Hanisch, R.J.V. Brissenden and J. Barnes (ASP Conference Series), 536
- Lacey, C., Guiderdoni, B., Rocca-Volmegange, B., and Silk, J. 1993, *ApJ*, 402, 15
- Lejeune, T., Cuisinier, F., and Buser, R. 1998, *A&AS*, 130, 65
- Lejeune, T., Cuisinier, F., and Buser, R. 1997, *A&AS*, 125, 229
- Liu, M.C., Charlot, S., and Graham, J.R. 2000, *ApJ*, in press
- MacKenty, J. et al. 1997, *NICMOS Instrument Handbook* (Baltimore: STScI)
- Malin, D.F., Quinn, P.J., and Graham, J.A. 1983, *ApJ*, 272, L5
- Marleau, F.R., Graham, J.R., Liu, M.C., and Charlot, S. 2000, in preparation
- Mathieu, A., Dejonghe, H., and Hui, X. 1996, *A&A*, 309, 30
- Minniti, D., Alonso, M.V., Goudfrooij, P., Jablonka, P., and Meylan, G. 1996, *ApJ*, 467, 221
- Najita, J., Dickinson, M., and Holfeltz, S. 1998, *Instrument Science Report NICMOS 98001*
- Persson, S.E., Frogel, J.A., and Aaronson, M. 1979, *ApJS*, 39, 61
- Pickles, A.J. 1998, *PASP*, 110, 863
- Quillen, A.C., Graham, J.R., and Frogel, J.A. 1993, *ApJ*, 412, 550
- Renzini, A. 1998, *AJ*, 115, 2459
- Rieke, M. April 1999, private communication
- Rieke, G. H., and Lebofsky, R. M. 1985, *ApJ*, 288, 618
- Schiminovich, D., van Gorkom, J.H., van der Hulst J.M., and Kasow, S. 1994, *ApJ*, 423, L101
- Shanks, T., Stevenson, P.R.F., Fong, R., and McGillivray, H.T. 1984, *MNRAS*, 206, 767
- Silva, D.R., and Bothun, G.D. 1998, *AJ*, 116, 85
- Somerville, R. 1997, PhD thesis, University of California at Santa Cruz
- Soria, R., Mould J.R., Watson A.M., et al. 1996, *ApJ*, 465, 79 (SMW96)
- Stetson, P.B. 1992, in *Astronomical Data Analysis Software and Systems I*, eds. D.M. Worrall, C. Biemesderfer, and J. Barnes (San Francisco ASP), ASP Conference Series, 25, 297

- Stetson, P.B., and Harris, P.B. 1988, *AJ*, 96, 909
- Stetson, P.B. 1987, *PASP*, 99, 191
- Tinsley, B.M., 1980, *ApJ*, 241, 41
- Tinsley, B.M., and Gunn, J.E. 1976, *ApJ*, 203, 52
- Thompson, R.I., Rieke, M., Schneider, G., Hines, D.C, and Corbin, M.R. 1998, *ApJ*, 492, L95
- Tokunaga, A.T. 1995, *Infrared Astronomy Chapter for a revised Astrophysical Quantities*, Cox, A.N., Editor.
- Tonry, J.L., Blakeslee, J.P., Ajhar, E.A., and Dressler, A. 1997, *ApJ*, 475, 399
- Tonry, J.L. 1991, *ApJ*, 373, L1
- Tonry, J.L., and Schechter P.L. 1990, *AJ*, 100, 1794
- Toomre, A. and Toomre, J. 1972, *ApJ*, 178, 623
- Tubbs, A.D. 1980, *ApJ*, 241, 969
- van den Bergh, S. 1976, *ApJ*, 208, 673
- Weil, M.L., and Hernquist, L. 1996, *ApJ*, 460, 101
- White, S.D.M., and Frenk, C.S. 1991, *ApJ*, 379, 52
- White, S.D.M., and Rees, M.J. 1978, *MNRAS*, 183, 341
- Worthey, G., Faber, S.M, and Gonzalez, J.J 1992, *ApJ*, 398, 69
- Yoshii, Y. and Takahara, F. 1988, *ApJ*, 326, 1

Fig. 1.— The HST field of view (FOV) of the NICMOS cameras (*solid squares*) overlaid on the Digital Sky Survey image $15'.0 \times 15'.0$ wide. From left to right, the *solid squares* represent NIC3, NIC1 and NIC2. The WFPC2 FOV of SMW96 is shown as the *dotted squares*. The geometric center of the NIC1+NIC2 combined FOV was chosen to coincide with the geometric center of the WFPC2 CHIP-3 FOV of SMW96. The NIC1+NIC2 FOV was chosen so that it falls inside the WFPC2 CHIP-3 FOV for any position angle.

Fig. 2.— NIC2 F110W (*top*) and F160W (*bottom*) mosaics. The *left* images show the reduced NIC2 mosaics in each filter. Each NIC2 mosaic covers a field of view $20''.4 \times 20''.4$ wide. The labels are in arcseconds and the grey scale represents counts per second. The *right* images show a $10''.2 \times 10''.2$ wide close up of the central region of the mosaics. The Airy rings are clearly visible around the unblended stars.

Fig. 3.— The histogram of number of matches between stars in the F110W and F160W images. Poisson error bars are plotted. The *solid line* is the adopted model describing the matching process, which assumes a Gaussian distribution of centroid errors and a uniform background of random matches (*dashed line*). Inspection of this histogram suggests that a natural cut off for the matching radius is 1 pixel. The model then indicate that 3% of our sample is matched with the wrong star.

Fig. 4.— The completeness functions for the F160W and F110W NIC2 observations. Completeness tests were performed by adding artificial stars to each individual image. Stars were simulated with magnitudes between 20.0 and 26.5, at a 0.1 mag interval. Each simulation consisted of adding 132 stars to the real image, corresponding to 10% of the stars recovered from the F160W image. The 50% completeness level occurs at [F110W]=24.5 and [F160W]=23.8, respectively.

Fig. 5.— *At the top:* The luminosity functions for stars detected in the F110W (*dashed lines*) and F160W (*solid lines*) image respectively, taking into account the edge and χ^2 cuts. *At the bottom:* The luminosity functions for each respective color image obtained after applying the matching criterion ($r_m = 1$ pixel). The *dotted* histogram labeled *Galactic* represents the expected number of foreground stars contaminating each magnitude bin in the F160W image based on the Galaxy model of Cohen (1993) scaled by a factor of 3.9 (see Table 4).

Fig. 6.— Magnitude systems transformations. The plot shows our adopted linear transformation (*solid line*) between the homogenized system of Bessell and Brett (1988) and NICMOS. The *filled circles* and *open lozenges* are synthetic magnitudes calculated on a Vega-based system for the dwarf and giant stars respectively in the Pickles (1998) spectral library. The *crosses* are the data for stars from the NICMOS photometric calibration campaign (STScI NICMOS calibration web page) that also have ground based measurements from Persson, Frogel and Aaronson (1979). The observational errors are smaller than the cross symbols used to plot the points. The Persson, Frogel and Aaronson (1979) data have been transformed from the original Las Campanas Observatory system to the Bessell and Brett system (BB).

Fig. 7.— The plot shows *on the left* the data points and the mean (points) and standard deviation

(error bars) for each magnitude interval. The dotted line *on the right* shows the total uncertainties measured from our artificial-star experiments. The lines join the mean value at each magnitude. The vertical error bars represent the mean of the DAOPHOT photometric errors for both the real data and the artificial-star tests. The *dashed line* defines the 50% completeness limit. The reddening vector has an amplitude of $E(J - H) = 0.04$ and $A_H = 0.06$ (smaller than the data points).

Fig. 8.— For each 0.5 magnitude bin in the range $[F160W]=20.5 - 24.0$, histogram showing the distribution of $[F110W]-[F160W]$ color for our NICMOS data. Overplotted on each histogram is a Gaussian fit using the mean and standard deviation calculated for each magnitude bin.

Fig. 9.— *On the left:* Comparison of our data (*filled circles*) with the 12 Gyr old stellar population isochrones of BC00. From left to right, BC00’s 12 Gyr isochrone for the metallicity $[Fe/H]=-1.7$, -0.7 , -0.4 , $+0.0$, and $+0.4$. Each individual *solid line* represents the RGB and each *dotted line* shows the AGB phase. *On the right:* CMD comparing our data to the red giant branches of globular clusters. From left to right, the *solid lines* are the loci of the giant branches of the four clusters M92, 47 Tuc, M67 and NGC 6553 with metallicities $[Fe/H]=-2.0$, -0.7 , -0.1 , and -0.3 , respectively.

Fig. 10.— *On the left:* Comparison of our data (*filled circles*) with the 12 Gyr old stellar population isochrones of Bertelli et al. (1994) (RGB only). From left to right, the 12 Gyr isochrone for the metallicity $[Fe/H]=-1.7$, -0.7 , -0.4 , $+0.0$, and $+0.4$. The upper parts of the $[Fe/H] \geq -1.7$ $(J - H)_{BB}$ isochrones (e.g., $[F160W] < 22.19$ or $M_{H_{BB}} < -5.59$ for $[Fe/H]=-0.7$) are not yet satisfactory according to Bertelli (1999), due to the problems in atmosphere models and scales of effective temperature for M giants. *On the right:* Comparison with the 12 Gyr old stellar population isochrones of BC00. Each individual *solid line* represents the RGB whereas each *dotted line* shows the AGB.

Fig. 11.— For each 0.5 magnitude bin in the range $[F160W]=21.0 - 24.0$, histogram showing the distribution of $[Fe/H]$ for the stars in our CMD with $[F160W]$ magnitudes fainter than the TRGBs of the 12 Gyr isochrones of BC00 (metallicity dependent; the brightest TRGB is at $[F160W]=21.2$) and with $[F110W]-[F160W]$ colors within the model predictions. The metallicities of individual stars can only be estimated for stars with $[Fe/H]=-1.7$ to $+0.4$ by using the 12 Gyr isochrones of BC00 and a simple linear interpolation method.

Fig. 12.— *Top panel:* Histogram showing the distribution of $[Fe/H]$ for the 353 stars in our CMD with $[F160W]$ magnitudes fainter than the TRGBs of the 12 Gyr isochrones of BC00 (metallicity dependent; the brightest TRGB is at $[F160W]=21.2$) and with $[F110W]-[F160W]$ colors within the model predictions. The peak of the Gaussian fit, over-plotted on the histogram, is at $[Fe/H]=-0.76$ with a dispersion of $\sigma = 0.44$. *Middle panel:* The $[Fe/H]$ distribution for the brightest halo field stars of HHP99 with magnitudes $I = 25.0 - 26.0$. The curve represents the Gaussian fit to our NICMOS data that has been re-normalized to the halo stars counts. *Bottom panel:* The $[Fe/H]$ distribution for 47 globular clusters in the halo of NGC 5128 ($R < 4'$; Harris et al. 1992). The

Gaussian curve fitted to our NICMOS data is over-plotted on the histogram, re-normalized to the globular cluster counts. The dispersion of the NICMOS halo stars $[\text{Fe}/\text{H}]$ distribution agrees well with the overall metallicity dispersion of the globular clusters and the halo stars of HHP99. The overall distribution does not seem to be resolved into multiple peaks, as is the case for the halo stars of HHP99 and the globular clusters.

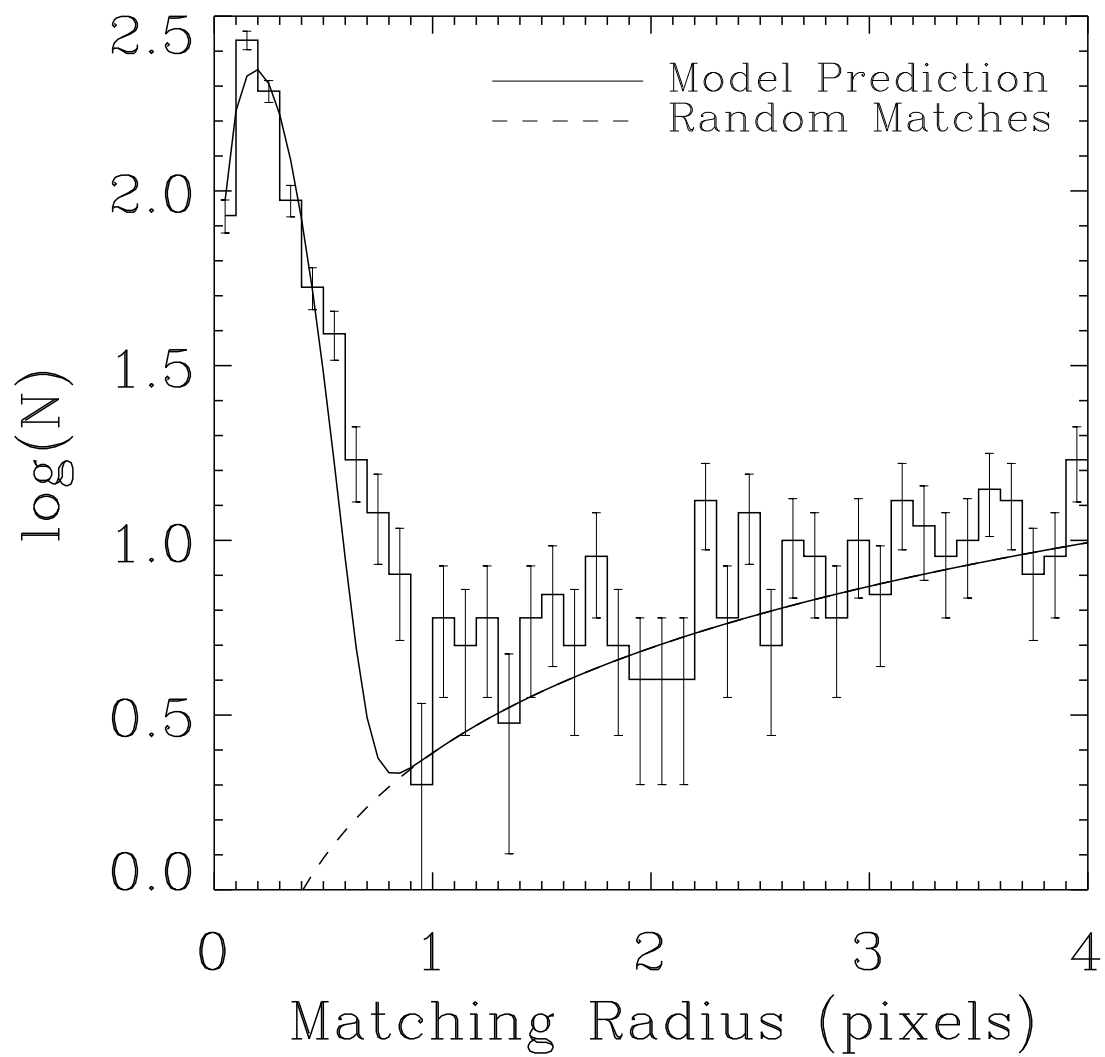
Fig. 13.— *On the left:* Comparison of our data (*filled circles*) with the 2 Gyr old stellar population isochrones of BC00. Each individual *solid line* represents the RGB whereas each *dotted line* shows the AGB. From left to right, the 2 Gyr isochrone for the metallicity $[\text{Fe}/\text{H}] = -1.7, -0.7, -0.4, +0.0$, and $+0.4$. The last point on the isochrones with metallicity $[\text{Fe}/\text{H}] = -0.7, -0.4$, and $+0.0$ is for the carbon AGB stars. The *long dashed* line represents a 5 Gyr old isochrone with solar metallicity, assuming a distance modulus of 15.0 for the Galactic stars contamination. The colors and magnitudes of the 5 brightest stars above the TRGB are consistent with being Galactic K–M dwarfs along our line of sight. *On the right:* Comparison of LMC+SMC AGB stars with our data. This shows that the presence of a young- to intermediate-age population would be revealed by stars 1 – 2 mag above our observed TRGB. The *small diagonal crosses* and *plus symbols* are LMC+SMC AGB M-type and C-type stars, respectively, with ages between 1 – 3 Gyr. The *large diagonal crosses* and *plus symbols* are LMC+SMC AGB M-type and C-type stars, respectively, with ages between 40 – 120 Myr.

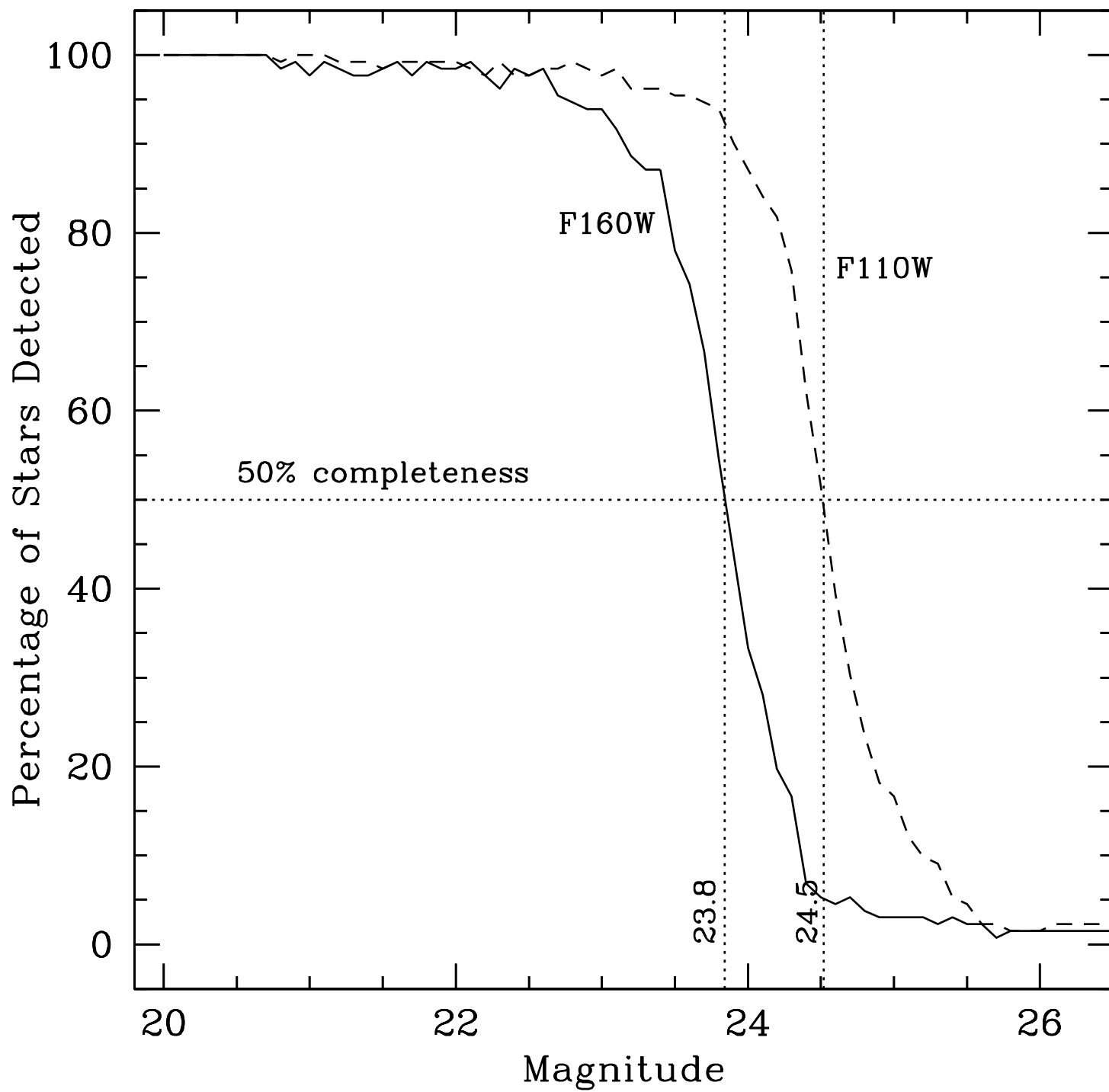
This figure "Marleau.fig1.jpg" is available in "jpg" format from:

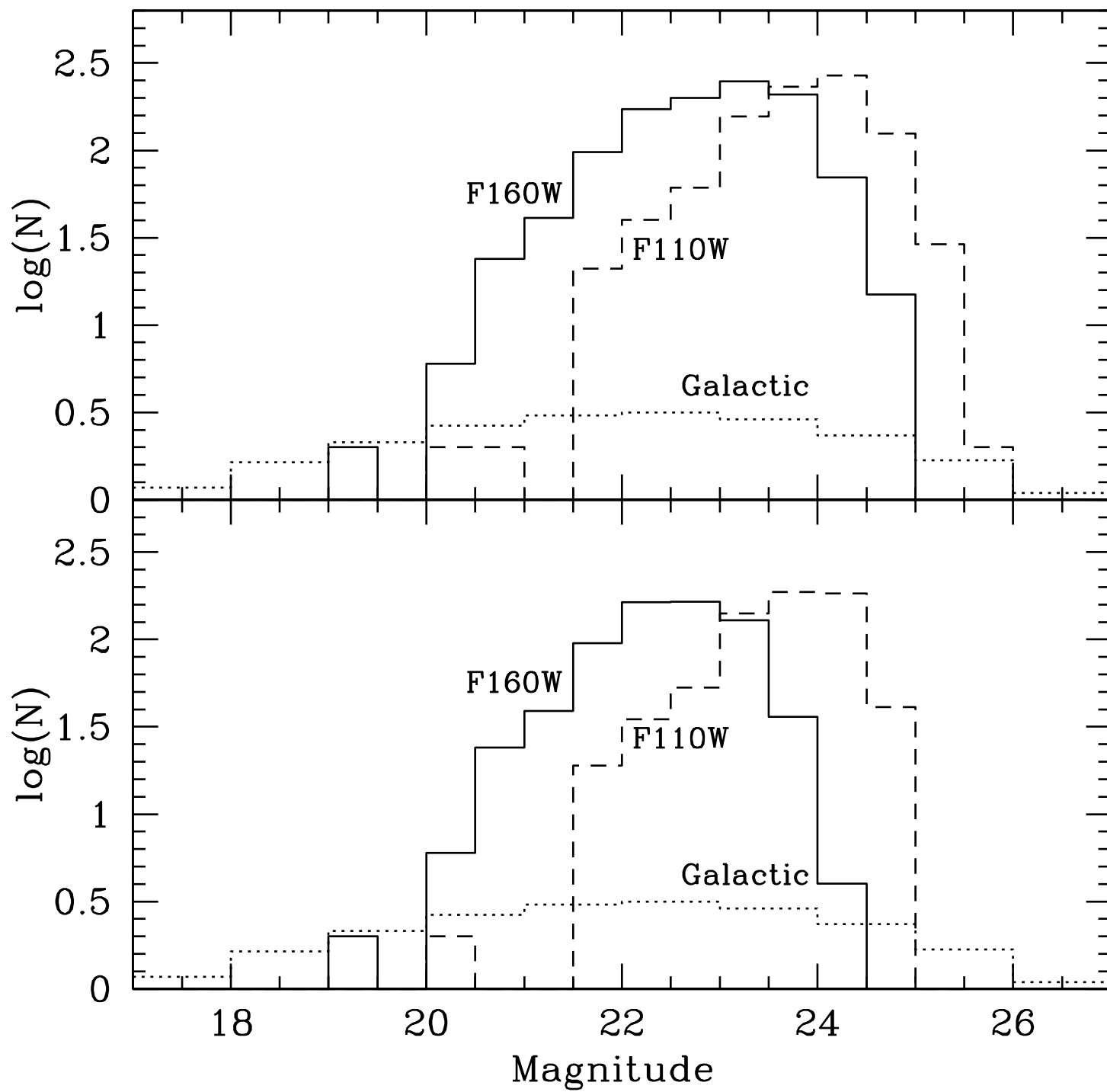
<http://arxiv.org/ps/astro-ph/0005305v1>

This figure "Marleau.fig2.jpg" is available in "jpg" format from:

<http://arxiv.org/ps/astro-ph/0005305v1>





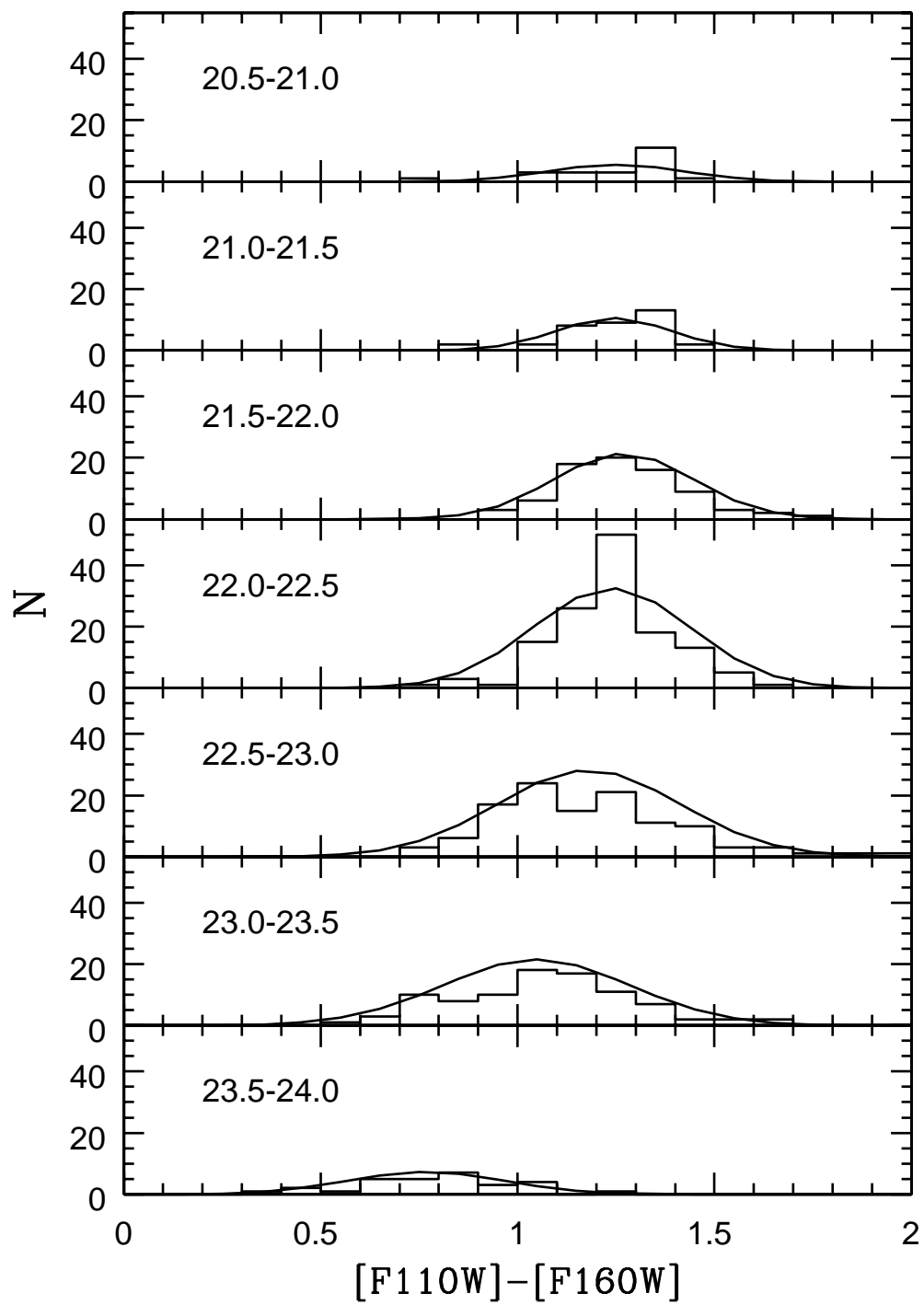


This figure "Marleau.fig6.jpg" is available in "jpg" format from:

<http://arxiv.org/ps/astro-ph/0005305v1>

This figure "Marleau.fig7.jpg" is available in "jpg" format from:

<http://arxiv.org/ps/astro-ph/0005305v1>

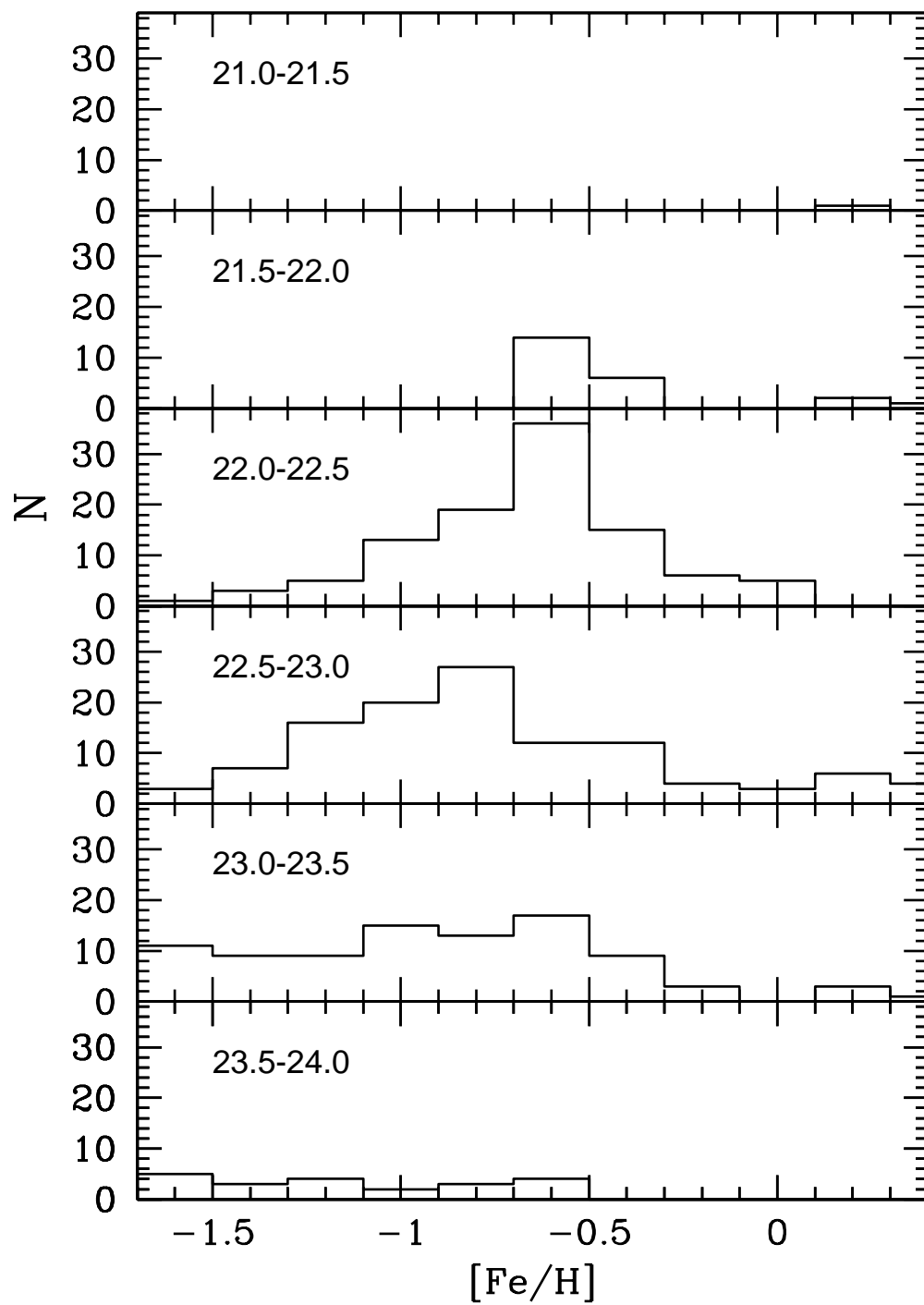


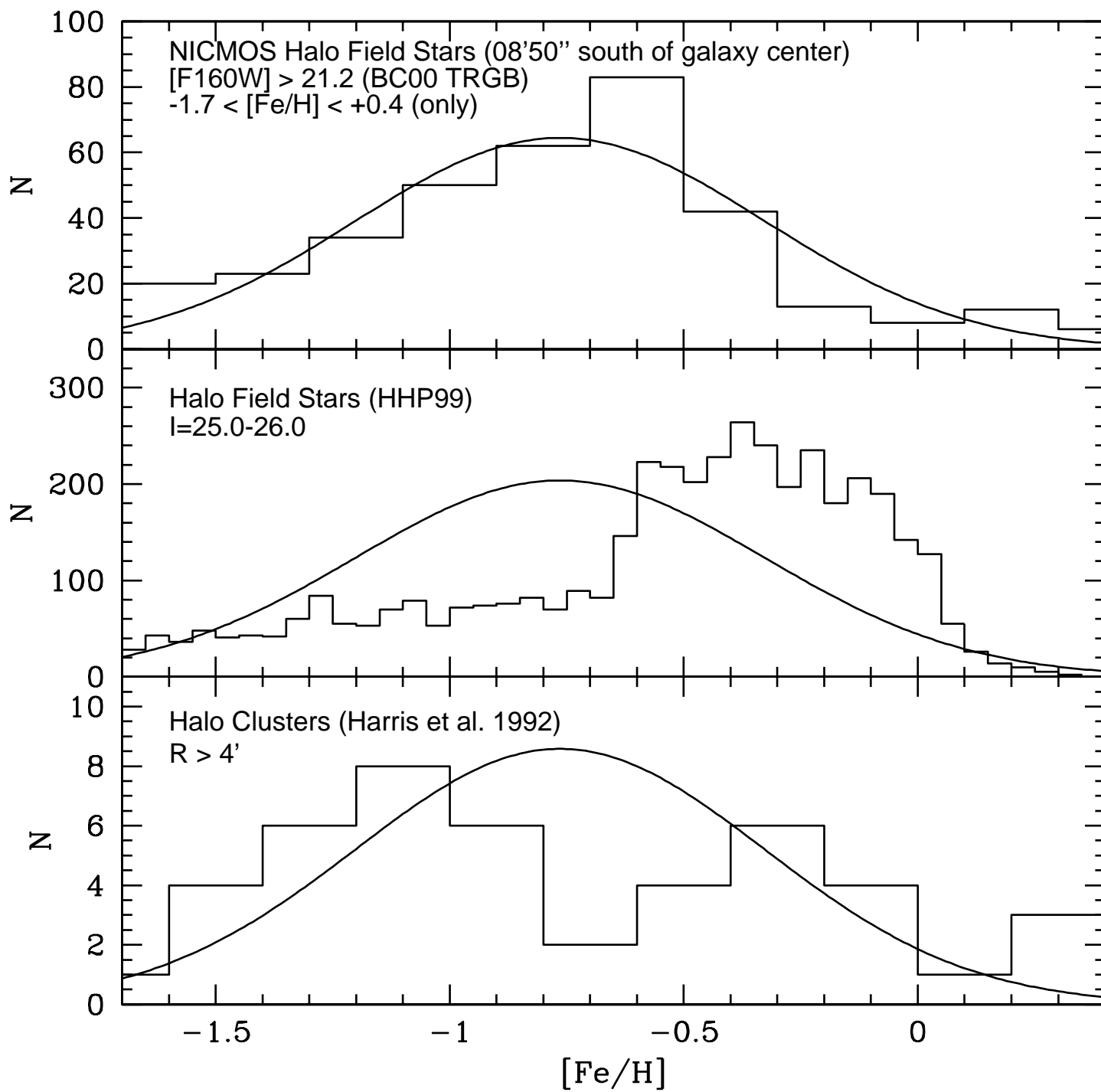
This figure "Marleau.fig9.jpg" is available in "jpg" format from:

<http://arxiv.org/ps/astro-ph/0005305v1>

This figure "Marleau.fig10.jpg" is available in "jpg" format from:

<http://arxiv.org/ps/astro-ph/0005305v1>





This figure "Marleau.fig13.jpg" is available in "jpg" format from:

<http://arxiv.org/ps/astro-ph/0005305v1>